

Compact and Three-dimensional Extension of Two-Stage Fourth-Order Gas-Kinetic Scheme

X. Ji*, L. Pan** and K. Xu*
Corresponding author: makxu@ust.hk

* Hong Kong University of Science and Technology, Hong Kong

** Institute of Applied Physics and Computational Mathematics, Beijing, China.

Abstract: Recently, a two-stage fourth-order (S2O4) gas-kinetic scheme (GKS) has been proposed for two-dimensional compressible Euler and Navier-Stokes equations on structured mesh [1]. In comparison with early one-step third-order (S1O3) GKS [2], the S2O4 GKS not only presents better accuracy and robustness, but also shows higher efficiency. The complexity of the algorithm has been greatly reduced. In this paper, further extension has been done to explore the potential of the S2O4 GKS framework. Firstly, the S2O4 GKS is naturally extended to calculate three-dimensional flow. Based on the three-dimensional WENO reconstruction and flux evaluation at Gaussian quadrature points, the high-order accuracy in space is fully achieved. The 3D S2O4 scheme has the preferred advantages as the 2D method, such as accuracy and efficiency for the complex flow computation. Secondly, a fourth-order compact gas-kinetic scheme (GKS) is developed for the two-dimensional flow on structured mesh. The scheme achieves compactness due to the availability of the time accurate evolution solution at cell interfaces under GKS framework. The Hermite WENO (HWENO) reconstruction is adopted to get higher-order spatial flow distributions with compact stencils. In comparison with compact fourth-order DG method, the current scheme uses only two stages instead of four within each time step for the fourth-order temporal accuracy, and the CFL number used here can be on the order of 0.5 instead of 0.11 for the DG method. Similarly, based on HWENO type reconstruction, a two-stage third-order compact GKS for unstructured triangular mesh is also constructed. Preliminary results for inviscid flow with strong shocks are shown.

Keywords: Gas-Kinetic Scheme, Two-Stage Fourth-Order Temporal Discretization, WENO, Hermite WENO, Unstructured Mesh.

1 Introduction

The gas-kinetic schemes (GKS) target on solving Euler and Navier-Stokes equations under finite volume framework [3]. Its flux is based on a time-dependent evolution solution of the kinetic model equation, such as the Bhatnagar-Gross-Krook (BGK) model [4]. High order gas kinetic schemes (HGKS) have been developed systematically in the past decades [5]. In comparison with traditional Riemann solver based high-order CFD methods, the distinguishable points of HGKS include the following: (i) The time evolving gas distribution function provides a multiple scale flow physics from the kinetic particle transport to the hydrodynamic wave propagation, which bridges the evolution from the upwind flux vector splitting to the central difference Lax-Wendroff type discretization. (ii) Both inviscid and viscous fluxes are obtained from the moments of a single gas distribution function. (iii) The GKS is intrinsically a multi-dimensional scheme [6], where both normal and tangential derivatives of flow variables around a cell interface participate the time evolution process of the gas distribution function. (iv) The time dependent gas distribution function along a cell interface provides a time evolution solution rather than a constant state in the Riemann solver, and this time dependent solution at a cell interface can be used to construct compact scheme. With the spatial and temporal coupled gas distribution function, a one-step 3rd-order scheme has been constructed [5]. Recently, with the multi-derivative multi-stage technique, a family of HGKS can be obtained [7]. Based

on the same 5th-order WENO reconstruction, the performance of HGKS shows advantages in terms of efficiency, accuracy, and robustness compared with traditional Riemann solver based high order schemes. Especially, HGKS can capture complicated flow structures i.e., shear instabilities, significantly better than than the schemes based on the Riemann solver due to the multi-dimensional property in GKS. Among the multi-derivative multi-stage GKS, the two-stage fourth-order GKS [1] seems to be an optimized choice in practical use, which is both efficient and accurate, and is as robust as 2nd-order scheme.

In this study, we present the recent progress in the GKS research. With the implementation of three-dimensional WENO reconstruction, two-stage fourth-order GKS is extended to three dimensional flows. In comparison with the early third-order three-dimensional scheme [8], the current fourth-order scheme reduces the complexity of the gas-kinetic solver greatly, and improves the robustness of scheme. Numerical results show that the current scheme has the same reliability and applicability as the well-developed second-order scheme, but is much more accurate and effective in capturing complicated flow structures. The current scheme provides state-of-art solutions from a higher-order scheme for simulations from the low-speed turbulence to the hypersonic flow. A two-stage fourth-order compact scheme has been developed as well. To achieve its compactness, a compact reconstruction based on the cell averaged and cell interface values is applied [9]. Besides updating the conservative flow variables inside each control volume, the time accurate solution from the GKS at a cell interface can be used as well. Inspired by the Hermite WENO (HWENO) reconstruction [10] and compact fourth-order GRP scheme [11], the HWENO reconstruction is implemented for the current compact GKS method. For engineering applications, the construction of higher-order numerical schemes on unstructured meshes becomes extremely demanding. After the successful validation of the compact GKS with HWENO reconstruction on structured mesh, a compact third-order GKS on unstructured mesh is presented as well.

This paper is organized as follows. A brief review for the finite volume GKS is given in Section 2. The formulation for the two-stage fourth-order time-accurate discretization is introduced in Section 3. The extensions of S2O4 GKS are listed in Section 4. We present the key procedures on implementing three dimensional S2O4 GKS in section 4.1. The construction of compact scheme is given in Section 4.2-4.4. Section 5 includes numerical examples to validate the current algorithms. The last section is the conclusion.

2 BGK equation and finite volume scheme

The second order GKS in finite volume framework is briefly summarized under two-dimensional case in this section. Systematic construction of GKS for 1-D to 3-D cases could be found in [12].

The 2-D BGK equation [4] can be written as

$$f_t + uf_x + vf_y = \frac{g - f}{\tau}, \quad (1)$$

where $\mathbf{u} = (u, v)$ is the particle velocity, f is the gas distribution function, g is the 2-D Maxwellian distribution, and τ is the collision time. The collision term satisfies the compatibility condition

$$\int \frac{g - f}{\tau} \psi d\Xi = 0, \quad (2)$$

where $\psi = (1, u, v, \frac{1}{2}(u^2 + v^2 + \xi^2))^T$, the internal variables ξ^2 equals to $\xi^2 = \xi_1^2 + \dots + \xi_K^2$, $d\Xi = dudvd\xi^1 \dots d\xi^K$, K is the internal degrees of freedom, and the specific heat ratio $\gamma = (K + 4)/(K + 2)$ for two-dimensional flows. In the continuum region, the gas distribution function can be expanded as

$$f = g - \tau D_{\mathbf{u}} g + \tau D_{\mathbf{u}} (\tau D_{\mathbf{u}}) g - \tau D_{\mathbf{u}} [\tau D_{\mathbf{u}} (\tau D_{\mathbf{u}}) g] + \dots,$$

where $D_{\mathbf{u}} = \frac{\partial}{\partial t} + \mathbf{u} \cdot \nabla$. Based on the Chapman-Enskog expansion, the macroscopic equations can be derived [3]. With the zeroth-order truncation

$$f = g,$$

the Euler equations can be obtained. With the first-order truncation

$$f = g - \tau(ug_x + vg_y + gt),$$

the Navier-Stokes equations can be obtained. With the higher order truncations, the Burnett and super-Burnett equations can be derived. Thus, in the gas-kinetic scheme, the Euler and Navier-Stokes solutions can be obtained according to the Chapman-Enskog expansion without solving the macroscopic equations.

Taking moments of Eq.(1) and integrating over the control volume $V_{ij} = \bar{x}_i \times \bar{y}_j$ with $\bar{x}_i = [x_i - \Delta x/2, x_i + \Delta x/2]$, $\bar{y}_j = [y_j - \Delta y/2, y_j + \Delta y/2]$, the semi-discretized finite volume scheme can be written as

$$\frac{dQ_{ij}}{dt} = \frac{1}{|V_{ij}|} \left[\int_{\bar{y}_j} (F_{i-1/2,j} - F_{i+1/2,j}) dy + \int_{\bar{x}_i} (G_{i,j-1/2} - G_{i,j+1/2}) dx \right], \quad (3)$$

where $Q = (\rho, \rho U, \rho V, \rho E)^T$ are the conservative flow variables, Q_{ij} is the cell averaged value over control volume V_{ij} and $|V_{ij}| = \Delta x \Delta y$. For the two-dimensional computation, the Gaussian quadrature for the numerical fluxes is used to achieve the accuracy in space, and the numerical fluxes in x -direction is given as an example

$$\int_{\bar{y}_j} F_{i+1/2,j} dy = \Delta y \sum_{m=1}^M \omega_m F(\mathbf{x}_{i+1/2,j_m}, t),$$

$\mathbf{x}_{i+1/2,m} = (x_{i+1/2}, y_{j_m})$. $y_{j_m}, m = 1, \dots, M$ are the Gauss quadrature points for \bar{y}_j and ω_m are quadrature weights. $M = 2$ is used in this paper to achieve up to fourth-order spatial accuracy. Based on the spatial reconstruction, which will be presented in the Section 4, the reconstructed point value and the spatial derivatives at each Gauss quadrature points can be obtained and the numerical fluxes $F(\mathbf{x}_{i+1/2,j_m}, t)$ can be provided by the flow solvers. In the gas-kinetic scheme, the numerical fluxes at the Gaussian quadrature point can be obtained by taking moments of the gas distribution function

$$F(\mathbf{x}_{i+1/2,j_m}, t) = \int \psi u f(\mathbf{x}_{i+1/2,j_m}, t, \mathbf{u}, \xi) du dv d\xi, \quad (4)$$

where $f(\mathbf{x}_{i+1/2,j_m}, t, \mathbf{u}, \xi)$ is provided by the integral solution of BGK equation Eq.(1) at the cell interface

$$f(\mathbf{x}_{i+1/2,j_m}, t, \mathbf{u}, \xi) = \frac{1}{\tau} \int_0^t g(\mathbf{x}', t', \mathbf{u}, \xi) e^{-(t-t')/\tau} dt' + e^{-t/\tau} f_0(-\mathbf{u}t, \xi), \quad (5)$$

where $\mathbf{x}_{i+1/2,j_m}$ is the location of cell interface, $x_{i+1/2} = x' + u(t-t')$, $y_{j_m} = y' + v(t-t')$ is the trajectory of particles, f_0 is the initial gas distribution and g is the corresponding equilibrium state. The 2-D second-order gas-kinetic solver [3] can be expressed as

$$\begin{aligned} f(\mathbf{x}_{i+1/2,j_m,k_n}, t, \mathbf{u}, \xi) = & (1 - e^{-t/\tau})g_0 + ((t + \tau)e^{-t/\tau} - \tau)(\bar{a}_1 u + \bar{a}_2 v)g_0 + (t - \tau + \tau e^{-t/\tau})\bar{A}g_0 \\ & + e^{-t/\tau}g_r[1 - (\tau + t)(a_{1r}u + a_{2r}v) - \tau A_r]H(u) \\ & + e^{-t/\tau}g_l[1 - (\tau + t)(a_{1l}u + a_{2l}v) - \tau A_l](1 - H(u)). \end{aligned} \quad (6)$$

With the second-order gas-kinetic solver Eq.(6), the second-order accuracy in time can be achieved by one step integration. In the one-stage gas evolution model, the third-order and fourth-order gas-kinetic solver has been developed as well. The formulation of one-stage gas-kinetic solvers, which can be found in [2], become very complicated, especially for the multidimensional computations [8]. Its complicated formulation in the one stage scheme has become a barrier for its further development to fourth- and fifth-orders.

3 Fourth-order temporal discretization

Recently, a two-stage fourth-order time-accurate discretization was developed for Lax-Wendroff flow solvers, particularly applied for hyperbolic equations with the generalized Riemann problem (GRP) solver [13] and

gas-kinetic scheme [1]. Such method provides a reliable framework to develop a fourth-order with a second-order time accurate flux function, i.e., Eq.(6). Consider the following time-dependent equation

$$\frac{\partial \mathbf{q}}{\partial t} = \mathcal{L}(\mathbf{q}), \quad (7)$$

with the initial condition at t_n , i.e.,

$$\mathbf{q}(t = t_n) = \mathbf{q}^n,$$

where \mathcal{L} is an operator for spatial derivative of flux. The time derivatives are obtained using the Cauchy-Kovalevskaya method,

$$\frac{\partial \mathbf{q}^n}{\partial t} = \mathcal{L}(\mathbf{q}^n), \quad \frac{\partial}{\partial t} \mathcal{L}(\mathbf{q}^n) = \frac{\partial}{\partial \mathbf{q}} \mathcal{L}(\mathbf{q}^n) \mathcal{L}(\mathbf{q}^n).$$

Introducing an intermediate state at $t^* = t_n + \Delta t/2$,

$$\mathbf{q}^* = \mathbf{q}^n + \frac{1}{2} \Delta t \mathcal{L}(\mathbf{q}^n) + \frac{1}{8} \Delta t^2 \frac{\partial}{\partial t} \mathcal{L}(\mathbf{q}^n), \quad (8)$$

the corresponding time derivatives are obtained as well for the intermediate stage state,

$$\frac{\partial \mathbf{q}^*}{\partial t} = \mathcal{L}(\mathbf{q}^*), \quad \frac{\partial}{\partial t} \mathcal{L}(\mathbf{q}^*) = \frac{\partial}{\partial \mathbf{q}} \mathcal{L}(\mathbf{q}^*) \mathcal{L}(\mathbf{q}^*).$$

Then, the state \mathbf{q} can be updated with the following formula,

$$\mathbf{q}^{n+1} = \mathbf{q}^n + \Delta t \mathcal{L}(\mathbf{q}^n) + \frac{1}{6} \Delta t^2 \left(\frac{\partial}{\partial t} \mathcal{L}(\mathbf{q}^n) + 2 \frac{\partial}{\partial t} \mathcal{L}(\mathbf{q}^*) \right). \quad (9)$$

It can be proved that for hyperbolic equations the above time stepping method (Eq.(8) and Eq.(9)) provides a fourth-order time accurate solution for $\mathbf{q}(t)$ at $t = t_n + \Delta t$. More details of the analysis can be found in [13].

Introduce the following time dependent function

$$\mathcal{L}(Q_{ij}) = \frac{1}{|V_{ij}|} \left[\int_{\bar{y}_j} (F_{i-1/2,j} - F_{i+1/2,j}) dy + \int_{\bar{x}_i} (G_{i,j-1/2} - G_{i,j+1/2}) dx \right],$$

Eq.(13) can be rewritten as

$$\frac{dQ_{ij}}{dt} = \mathcal{L}(Q_{ij}).$$

Then the semi-discretized finite volume scheme becomes a particular case of the general ODE system. The two-stage method in Eq.(8) and Eq.(9) can be extended directly for Eq.(13). For the gas-kinetic scheme, the gas evolution is a relaxation process from kinetic to hydrodynamic scale through the exponential function, and the corresponding flux is a complicated function of time. In order to obtain the time derivatives of the flux function at t_n and $t_* = t_n + \Delta t/2$ with the correct physics, the flux function should be approximated as a linear function of time within a time interval. According to the numerical fluxes at the Gauss quadrature points in Eq.(4), the following notation is introduced

$$\mathbf{F}_{i+1/2,j}(Q^n, t) = \sum_{m=1}^M \omega_m F(\mathbf{x}_{i+1/2,j_m}, t),$$

and

$$\mathbb{F}_{i+1/2,j}(Q^n, \delta) = \int_{t_n}^{t_n + \delta} \mathbf{F}_{i+1/2,j}(Q^n, t) dt,$$

where $F(\mathbf{x}_{i+1/2,j_m}, t)$ is obtained according to Eq.(4). In the time interval $[t_n, t_n + \Delta t]$, the flux is expanded as the following linear form

$$\mathbf{F}_{i+1/2,j}(Q^n, t) = \mathbf{F}_{i+1/2,j}^n + \partial_t \mathbf{F}_{i+1/2,j}^n (t - t_n).$$

The coefficients $\mathbf{F}_{i+1/2,j}(Q^n, t_n)$ and $\partial_t \mathbf{F}_{i+1/2,j}(Q^n, t_n)$ can be determined as follows,

$$\begin{aligned} \mathbf{F}_{i+1/2,j}(Q^n, t_n) \Delta t + \frac{1}{2} \partial_t \mathbf{F}_{i+1/2,j}(Q^n, t_n) \Delta t^2 &= \mathbb{F}_{i+1/2,j,k}(Q^n, \Delta t), \\ \frac{1}{2} \mathbf{F}_{i+1/2,j}(Q^n, t_n) \Delta t + \frac{1}{8} \partial_t \mathbf{F}_{i+1/2,j}(Q^n, t_n) \Delta t^2 &= \mathbb{F}_{i+1/2,j}(Q^n, \Delta t/2). \end{aligned}$$

By solving the linear system, we have

$$\begin{aligned} \mathbf{F}_{i+1/2,j}(Q^n, t_n) &= (4\mathbb{F}_{i+1/2,j}(Q^n, \Delta t/2) - \mathbb{F}_{i+1/2,j}(Q^n, \Delta t)) / \Delta t, \\ \partial_t \mathbf{F}_{i+1/2,j}(Q^n, t_n) &= 4(\mathbb{F}_{i+1/2,j}(Q^n, \Delta t) - 2\mathbb{F}_{i+1/2,j}(Q^n, \Delta t/2)) / \Delta t^2. \end{aligned}$$

Similarly, the numerical fluxes $\mathcal{G}_{i,j+1/2}^n$ in the y -direction can be obtained as well. With the numerical fluxes and temporal derivatives, $\mathcal{L}(Q_{ij}^n)$ and $\mathcal{L}_t(Q_{ij}^n)$ can be given as follows

$$\begin{aligned} \mathcal{L}(Q_{ij}^n) &= \frac{1}{\Delta x} (\mathbf{F}_{i+1/2,j}(Q^n, t_n) - \mathbf{F}_{i-1/2,j}(Q^n, t_n)) \\ &\quad + \frac{1}{\Delta y} (\mathbf{G}_{i,j+1/2}(Q^n, t_n) - \mathbf{G}_{i,j-1/2}(Q^n, t_n)), \end{aligned} \quad (10)$$

$$\begin{aligned} \mathcal{L}_t(Q_{ij}^n) &= \frac{1}{\Delta x} (\partial_t \mathbf{F}_{i+1/2,j}(Q^n, t_n) - \partial_t \mathbf{F}_{i-1/2,j}(Q^n, t_n)) \\ &\quad + \frac{1}{\Delta y} (\partial_t \mathbf{G}_{i,j+1/2}(Q^n, t_n) - \partial_t \mathbf{G}_{i,j-1/2}(Q^n, t_n)). \end{aligned} \quad (11)$$

According to Eq.(8), Q_{ij}^* at t_* can be updated. With the similar procedure, the numerical fluxes and temporal derivatives at the intermediate stage can be constructed and $\mathcal{L}_t(Q_{ij}^*)$ is given by

$$\begin{aligned} \mathcal{L}_t(Q_{ij}^*) &= \frac{1}{\Delta x} (\partial_t \mathbf{F}_{i+1/2,j}(Q^*, t_*) - \partial_t \mathbf{F}_{i-1/2,j}(Q^*, t_*)) \\ &\quad + \frac{1}{\Delta y} (\partial_t \mathbf{G}_{i,j+1/2}(Q^*, t_*) - \partial_t \mathbf{G}_{i,j-1/2}(Q^*, t_*)). \end{aligned} \quad (12)$$

According to Eq.(10), Eq.(11), and Eq.(12), Q_{ij}^{n+1} at t_{n+1} can be updated by Eq.(9).

4 Spatial reconstruction

Before introducing the reconstruction procedure, let's denote \bar{Q} as cell averaged, \hat{Q} as line averaged, and Q as pointwise values. And we denote \tilde{Q} as surface averaged values in 3-D case. Here $Q^{l,r}$ represent the reconstructed quantities on the left and right sides, which correspond to the non-equilibrium initial part in GKS framework. Then, Q^e is the reconstructed equilibrium state.

4.1 Extension to three dimensional simulation

The construction of three-dimensional gas distribution function is straightforward based on the three dimensional BGK equation. The details could be found in [12, 8]. Within the control volume $V_{ijk} = \bar{x}_i \times \bar{y}_j \times \bar{z}_k$ with $\bar{x}_i = [x_i - \Delta x/2, x_i + \Delta x/2]$, $\bar{y}_j = [y_j - \Delta y/2, y_j + \Delta y/2]$, $\bar{z}_k = [z_k - \Delta z/2, z_k + \Delta z/2]$, the semi-discretized

finite volume scheme can be written as

$$\begin{aligned} \frac{dQ_{ijk}}{dt} = \frac{1}{|V_{ijk}|} & \left[\int_{\bar{y}_j \times \bar{z}_k} (F_{i-1/2,j,k} - F_{i+1/2,j,k}) dy dz \right. \\ & + \int_{\bar{x}_i \times \bar{z}_k} (G_{i,j-1/2,k} - G_{i,j+1/2,k}) dx dz \\ & \left. + \int_{\bar{x}_i \times \bar{y}_j} (H_{i,j,k-1/2} - H_{i,j,k+1/2}) dx dy \right], \end{aligned} \quad (13)$$

where $Q = (\rho, \rho U, \rho V, \rho W, \rho E)^T$ are the conservative flow variables, Q_{ijk} is the cell averaged value over control volume V_{ijk} and $|V_{ijk}| = \Delta x \Delta y \Delta z$.

The above time evolution solution is based on the high-order initial reconstruction for macroscopic flow variables and WENO reconstruction [14, 15] is adopted for the spatial reconstruction. For the three dimensional computation, the reconstruction procedure for the cell interface $x_{i+1/2,j,k}$ is given as an example. The point value Q_l, Q_r and Q_0 and first-order derivatives at the Gauss quadrature points $(x_{i+1/2}, y_{j_m}, z_{k_n})$, $m, n = 1, \dots, 2$ need to be constructed. The detailed procedure is given as follows

1. According to one dimensional reconstruction, the surface averaged reconstructed values

$$(\tilde{Q}^l)_{j-\ell_1, k-\ell_2}, (\tilde{Q}^r)_{j-\ell_1, k-\ell_2}, (\tilde{Q}^e)_{j-\ell_1, k-\ell_2},$$

and surface averaged spatial derivatives

$$(\partial_x \tilde{Q}^l)_{j-\ell_1, k-\ell_2}, (\partial_x \tilde{Q}^r)_{j-\ell_1, k-\ell_2}, (\partial_x \tilde{Q}^e)_{j-\ell_1, k-\ell_2},$$

can be constructed, where $\ell_1, \ell_2 = -2, \dots, 2$.

2. With the one-dimensional WENO reconstruction in the horizontal direction, the line averaged value

$$(\hat{Q}^l)_{j_m, k-\ell_2}, (\hat{Q}^r)_{j_m, k-\ell_2}, (\hat{Q}^e)_{j_m, k-\ell_2},$$

and the line averaged spatial derivatives

$$\begin{aligned} (\partial_x \hat{Q}^l)_{j_m, k-\ell_2}, (\partial_x \hat{Q}^r)_{j_m, k-\ell_2}, (\partial_x \hat{Q}^e)_{j_m, k-\ell_2}, \\ (\partial_y \hat{Q}^l)_{j_m, k-\ell_2}, (\partial_y \hat{Q}^r)_{j_m, k-\ell_2}, (\partial_y \hat{Q}^e)_{j_m, k-\ell_2} \end{aligned}$$

over the interval $[z_{k-\ell_2} - \Delta z/2, z_{k-\ell_2} + \Delta z/2]$ with $y = y_{j_m}$ can be given.

3. With one-dimensional WENO reconstruction in the vertical direction, the point value

$$(Q^l)_{j_m, k_n}, (Q^r)_{j_m, k_n}, (Q^e)_{j_m, k_n},$$

and spatial derivatives

$$\begin{aligned} (\partial_x Q^l)_{j_m, k_n}, (\partial_x Q^r)_{j_m, k_n}, (\partial_x Q^e)_{j_m, k_n}, \\ (\partial_y Q^l)_{j_m, k_n}, (\partial_y Q^r)_{j_m, k_n}, (\partial_y Q^e)_{j_m, k_n}, \\ (\partial_z Q^l)_{j_m, k_n}, (\partial_z Q^r)_{j_m, k_n}, (\partial_z Q^e)_{j_m, k_n}, \end{aligned}$$

can be fully given at the Gaussian quadrature points $(x_{i+1/2}, y_{j_m}, z_{k_n})$.

4. With the reconstructed point value and spatial derivatives at each Gaussian quadrature point $(x_{i+1/2}, y_{j_m}, z_{k_n})$, the corresponding numerical fluxes can be obtained by Eq.(4) and Eq.(6).

In the computation, without special statement, the fifth-order WENO-JS reconstruction [14] is adopted for the flow with discontinuities and the linear scheme is used for the smooth flows to reduce the dissipation.

4.2 Slope reconstruction inside each control volume

Different from the Riemann problem with a constant state at a cell interface, a time evolution solution is provided by the gas-kinetic scheme. Taking moments of the time-dependent gas distribution function, the pointwise values at a cell interface can be obtained

$$Q_{i+1/2,j_\ell}(t) = \int \psi f(x_{i+1/2}, y_{j_\ell}, t, u, v, \xi) du dv d\xi. \quad (14)$$

With the pointwise values at a cell interface, the cell averaged spatial derivatives for all flow variables are provided by the Green-Gauss theorem

$$\begin{aligned} \bar{Q}_x &= \frac{1}{\Delta S} \oint_{\Gamma} Q dy = \frac{1}{\Delta S} \sum_{k=0}^K \sum_{m=1}^2 Q_{k,m} \cos \alpha_k L_k, \\ \bar{Q}_y &= -\frac{1}{\Delta S} \oint_{\Gamma} Q dx = -\frac{1}{\Delta S} \sum_{k=0}^K \sum_{m=1}^2 Q_{k,m} \cos \beta_k L_k, \end{aligned} \quad (15)$$

where k is the index of edges of each cells, $K = 3$ for triangular and $K = 4$ for quadrangle, $\cos \alpha_k$ is angle of tangential direction of each edges with y positive direction, $\cos \beta_k$ is angle of tangential direction of each edges with x positive direction, and L_k is the length of each edges. As a particular example, Eq.(15) for one-dimensional flow reduces to

$$(\bar{Q}_x)_i = \frac{1}{\Delta x} \int_{I_i} \frac{\partial Q}{\partial x} dx = \frac{1}{\Delta x} (Q_{i+1/2} - Q_{i-1/2}),$$

and Eq.(15) for two-dimensional flow on structured meshes reduces to

$$\begin{aligned} (\bar{Q}_x)_{i,j} &= \frac{1}{\Delta x} \sum_{m=1}^2 (Q_{i+1/2,j_m} - Q_{i-1/2,j_m}), \\ (\bar{Q}_y)_{i,j} &= \frac{1}{\Delta y} \sum_{m=1}^2 (Q_{i_m,j+1/2} - Q_{i_m,j-1/2}). \end{aligned}$$

In order to utilize the pointwise values at cell interface in the spatial reconstruction, the temporal accuracy needs to be kept. Similar to the proposition for the two-stage temporal discretization, we have the following proposition for the time dependent gas distribution function at a cell interface

Proposition: *With the introduction of an intermediate state at $t_* = t_n + A\Delta t$,*

$$f^* = f^n + A\Delta t f_t^n + \frac{1}{2} A^2 \Delta t^2 f_{tt}^n, \quad (16)$$

the state f^{n+1} is updated with the following formula

$$f^{n+1} = f^n + \Delta t (B_0 f_t^n + B_1 f_t^*) + \frac{1}{2} \Delta t^2 (C_0 f_{tt}^n + C_1 f_{tt}^*), \quad (17)$$

and the solution f^{n+1} at $(t = t_n + \Delta t)$ has fourth-order accuracy with the following coefficients

$$A = \frac{1}{2}, B_0 = 1, B_1 = 0, C_0 = \frac{1}{3}, C_1 = \frac{2}{3}. \quad (18)$$

The proposition can be proved using the expansion

$$f^{n+1} = f^n + \Delta t f_t^n + \frac{\Delta t^2}{2} f_{tt}^n + \frac{\Delta t^3}{6} f_{ttt}^n + \frac{\Delta t^4}{24} f_{tttt}^n + \mathcal{O}(\Delta t^5).$$

According to the definition of the intermediate state, the above expansion becomes

$$\begin{aligned} f^{n+1} - f^n &= \Delta t(B_0 + B_1)f_t^n + \frac{\Delta t^2}{2}(C_0 + C_1 + 2B_1A)f_{tt}^n \\ &+ \frac{\Delta t^3}{2}(B_1A^2 + C_1A)f_{ttt}^n + \frac{\Delta t^4}{4}C_1A^2f_{tttt}^n + \mathcal{O}(\Delta t^5). \end{aligned}$$

To have a fourth-order accuracy for the interface value at t^{n+1} , the coefficients are uniquely determined by Eq.(18).

In order to utilize the two-stage fourth-order temporal discretization for the gas distribution function, the third-order gas-kinetic solver is needed [2, 16]. To construct the first and second order derivatives of the gas distribution function, the distribution function in Eq.(5) is approximated by the quadratic function

$$f(t) = f(x_{i+1/2}, y_{j\epsilon}, t, u, v, \xi) = f^n + f_t^n(t - t^n) + \frac{1}{2}f_{tt}^n(t - t^n)^2.$$

According to the gas-distribution function at $t = 0, \Delta t/2$, and Δt

$$\begin{aligned} f^n &= f(0), \\ f^n + \frac{1}{2}f_t^n \Delta t + \frac{1}{8}f_{tt}^n \Delta t^2 &= f(\Delta t/2), \\ f^n + f_t^n \Delta t + f_{tt}^n \Delta t^2 &= f(\Delta t), \end{aligned}$$

the coefficients f^n, f_t^n and f_{tt}^n can be determined

$$\begin{aligned} f^n &= f(0), \\ f_t^n &= (4f(\Delta t/2) - 3f(0) - f(\Delta t))/\Delta t, \\ f_{tt}^n &= 4(f(\Delta t) + f(0) - 2f(\Delta t/2))/\Delta t^2. \end{aligned}$$

Thus, f^* and f^{n+1} are fully determined at the cell interface. Therefore, the macroscopic variables $Q_{i+1/2}^{n+1}$ at a cell interface can be obtained by taking moments of f^{n+1} and the cell interface values can be used for the reconstruction at the beginning of next time step.

4.3 HWENO Reconstruction on structured mesh

For the one-dimensional reconstruction, three sub-stencils for cell I_i are selected

$$S_0 = \{I_{i-1}, I_i\}, \quad S_1 = \{I_i, I_{i+1}\}, \quad S_2 = \{I_{i-1}, I_i, I_{i+1}\}.$$

The Hermite quadratic reconstruction polynomials $w_i(x)$ corresponding to the substencil $S_i, i = 0, 1, 2$ are constructed according to the following conditions

$$\begin{aligned} \frac{1}{\Delta x} \int_{I_{i-j}} q_0(x) dV &= \bar{Q}_{i-j}, \quad j = 0, 1, & \frac{1}{\Delta x} \int_{I_{i-1}} q'_0(x) dV &= (\bar{Q}_x)_{i-1}, \\ \frac{1}{\Delta x} \int_{I_{i+j}} q_1(x) dV &= \bar{Q}_{i+j}, \quad j = 0, 1, & \frac{1}{\Delta x} \int_{I_{i+1}} q'_1(x) dV &= (\bar{Q}_x)_{i+1}, \\ \frac{1}{\Delta x} \int_{I_{i+j}} q_2(x) dV &= \bar{Q}_{i+j}, \quad j = -1, 0, 1. \end{aligned}$$

and the pointwise value at the cell interface $x_{i+1/2}$ can be given in terms of the cell averages value and the averaged spatial derivative as follows

$$\begin{aligned} q_0(x_{i+1/2}) &= -\frac{7}{6}\bar{Q}_{i-1} + \frac{13}{6}Q_i + \frac{2\Delta x}{3}(\bar{Q}_x)_{i-1}, \\ q_1(x_{i+1/2}) &= \frac{1}{6}\bar{Q}_i + \frac{5}{6}Q_i + \frac{\Delta x}{3}(\bar{Q}_x)_{i+1}, \\ q_2(x_{i+1/2}) &= -\frac{1}{6}\bar{Q}_{i-1} + \frac{5}{6}Q_i + \frac{1}{3}\bar{Q}_{i+1}. \end{aligned}$$

On the bigger stencil $\mathbb{T} = \{S_0, S_1, S_2\}$, a fourth-degree reconstruction polynomial $Q(x)$ are constructed according to the following conditions

$$\begin{aligned} \frac{1}{\Delta x} \int_{I_{i+j}} Q(x) dV &= \bar{Q}_{i+j}, \quad j = -1, 0, 1, \\ \frac{1}{\Delta x} \int_{I_{i+j}} Q'(x) dV &= (\bar{Q}_x)_{i+j}, \quad j = -1, 1, \end{aligned}$$

and the point value at the cell interface $x_{i+1/2}$ can be written as

$$Q(x_{i+1/2}) = -\frac{23}{120}\bar{Q}_{i-1} + \frac{19}{30}\bar{Q}_i + \frac{67}{120}\bar{Q}_{i+1} - \Delta x \left(\frac{3}{40}(\bar{Q}_x)_{i-1} + \frac{7}{40}(\bar{Q}_x)_{i+1} \right).$$

Similar to the classical WENO reconstruction, the linear weights $\gamma_k, k = 0, 1, 2$ can be found such that

$$Q(x_{i+1/2}) = \sum_{k=0}^2 \gamma_k q_k(x_{i+1/2}),$$

where $\gamma_0 = \frac{9}{80}, \gamma_1 = \frac{21}{40}, \gamma_2 = \frac{29}{80}$. To deal with the discontinuity, the normalized nonlinear weight is introduced as follows

$$\omega_k = \frac{\bar{\omega}_k}{\sum_p \bar{\omega}_p},$$

where the non-normalized nonlinear weights $\bar{\omega}_i$. The non-normalized weights $\bar{\omega}_i$ is defined as follows

$$\bar{\omega}_k = \frac{\gamma_k}{(\beta_k + \epsilon)^2},$$

where β_k are the smoothness indicators. Thus, the reconstructed left interface value $Q_{i+1/2}^l$ can be written as

$$Q_{i+1/2}^l = \sum_{k=0}^2 \bar{\omega}_k q_k(x_{i+1/2}).$$

Similarly, the reconstructed right interface value $Q_{i+1/2}^r$ can be constructed as well. More details of one-dimensional HWENO scheme can be found in [10]. With the reconstructed $Q_{i+1/2}^l$ and $Q_{i+1/2}^r$ at both sides of a cell interface $x_{i+1/2}$, the macroscopic variables $Q_{i+1/2}^e$ and the corresponding equilibrium state g_0 can be determined according to the compatibility condition [3]. To fully determine the slopes of the equilibrium state across the cell interface, the conservative variables across the cell interface are expanded as

$$Q^e(x) = Q_{i+1/2}^e + S_1(x - x_{i+1/2}) + \frac{1}{2}S_2(x - x_{i+1/2})^2 + \frac{1}{6}S_3(x - x_{i+1/2})^3 + \frac{1}{24}S_4(x - x_{i+1/2})^4.$$

With the following conditions,

$$\int_{I_{i+k}} Q^e(x) = \bar{Q}_{i+k}, k = -1, \dots, 2,$$

the derivatives are given by

$$\begin{aligned} (Q_x^e)_{i+1/2} = S_1 &= \left[-\frac{1}{12}(\bar{Q}_{i+2} - \bar{Q}_{i-1}) + \frac{5}{4}(\bar{Q}_{i+1} - \bar{Q}_i) \right] / \Delta x, \\ (Q_{xx}^e)_{i+1/2} = S_2 &= \left[-\frac{1}{8}(\bar{Q}_{i+2} + \bar{Q}_{i-1}) + \frac{31}{8}(\bar{Q}_{i+1} + \bar{Q}_i) - \frac{15}{2}Q_{i+1/2}^e \right] / \Delta x^2. \end{aligned} \quad (19)$$

Thus, the reconstruction for the initial data and the equilibrium part are fully given in the one-dimensional case.

For the two-dimensional reconstruction, the HWENO reconstruction can be extended by the strategy of direction by direction reconstruction. For the fourth-order scheme, two Gaussian points in each interface are needed for numerical flux integration. Our target is to construct

$$\begin{aligned} &Q^l, Q_x^l, Q_y^l, Q_{xx}^l, Q_{yy}^l, Q_{xy}^l, \\ &Q^r, Q_x^r, Q_y^r, Q_{xx}^r, Q_{yy}^r, Q_{xy}^r, \\ &Q^e, Q_x^e, Q_y^e, Q_{xx}^e, Q_{yy}^e, Q_{xy}^e, \end{aligned}$$

at each Gaussian point. To obtain these quantities, four line averaged slopes $(\hat{Q}_x)_{i,j_l}$, $(\hat{Q}_x)_{i_l,j}$ are additionally evaluated, where $l = 1, 2$ represents the location Gaussian quadrature points in the corresponding direction. The reconstruction procedure for the Gaussian point $(i - 1/2, j_1)$ is summarized as follows

1. To obtain the line average values, i.e. \hat{Q}_{i,j_l} , we perform HWENO reconstruction in tangential direction by using $\bar{Q}_{i,j-1}$, $\bar{Q}_{i,j}$, $\bar{Q}_{i,j+1}$, and $(\bar{Q}_y)_{i,j-1}$, $(\bar{Q}_y)_{i,j+1}$.
2. With the reconstructed line average values \hat{Q}_{i-1,j_1} , \hat{Q}_{i,j_1} , \hat{Q}_{i+1,j_1} and $(\hat{Q}_x)_{i-1,j_1}$, $(\hat{Q}_x)_{i+1,j_1}$, the one-dimensional HWENO method is used, and $Q_{i-1/2,j_1}^r$, $Q_{i+1/2,j_1}^l$ are obtained. $(Q_x^r)_{i-1/2,j_1}$, $(Q_x^l)_{i+1/2,j_1}$ and $(Q_{xx}^r)_{i-1/2,j_1}$, $(Q_{xx}^l)_{i+1/2,j_1}$ are constructed with the same derivative reconstruction method in [2].
3. The variables $Q_{i-1/2,j_1}^e$ at each Gaussian point can be obtained according to $Q_{i-1/2,j_1}^l$, $Q_{i-1/2,j_1}^r$ and the compatibility condition. $(Q_x^e)_{i-1/2,j_1}$, $(Q_{xx}^e)_{i-1/2,j_1}$ are calculated by Eq. (19).
4. For the tangential derivatives $(Q_y^r)_{i-1/2,j_1}$, $(Q_{yy}^r)_{i-1/2,j_1}$, a WENO-type reconstruction is adopted by using $Q_{i-1/2,(j-1)_2}^r$, $Q_{i-1/2,j_1}^r$, $Q_{i-1/2,j_2}^r$, $Q_{i-1/2,(j+1)_1}^r$. The derivatives $(Q_{xy}^r)_{i-1/2,j_1}$ could be obtained in the same way with corresponding Q_x^r .
5. A smooth third-order polynomial can be constructed by $Q_{i-1/2,(j-1)_2}^e$, $Q_{i-1/2,j_1}^e$, $Q_{i-1/2,j_2}^e$, $Q_{i-1/2,(j+1)_1}^e$ for the equilibrium part, and the tangential derivatives $(Q_y^e)_{i-1/2,j_1}$, $(Q_{yy}^e)_{i-1/2,j_1}$ are obtained. Similarly, $(Q_{xy}^e)_{i-1/2,j_1}$ can be determined by the corresponding Q_x^e .

Similar procedure can be performed to obtain all needed values at each Gaussian point.

4.4 HWENO Reconstruction on unstructured mesh

In this section, the HWENO Reconstruction will be extended to the unstructured mesh. A compact stencil for 2-D triangular mesh includes the targeted cell and its three neighboring cells. We indicate them as cell 0, 1, 2, 3 respectively. As a starting point of HWENO type reconstruction, a linear reconstruction will be presented. For a piecewise smooth function $Q(x, y)$ over cell Ω_i , a polynomial $P^r(x, y)$ with degree r can be constructed to approximate $Q(x, y)$ as follows

$$P^r(x, y) = Q(x, y) + O(\Delta x^{r+1}, \Delta y^{r+1}).$$

In order to achieve the third-order accuracy and satisfy conservative property, the following quadratic polynomial on the cell Ω_{i_0} is constructed

$$P^2(x, y) = Q_{i_0} + \sum_{k=1}^5 a_k p^k(x, y), \quad (20)$$

where Q_{i_0} is the cell average value of $Q(x, y)$ over cell Ω_{i_0} and $p^k(x, y)$, $k = 1, \dots, 5$ are basis functions, which are given as follows

$$\begin{cases} p^1(x, y) = x - \frac{1}{|\Omega_{i_0}|} \iint_{\Omega_{i_0}} x dx dy, \\ p^2(x, y) = y - \frac{1}{|\Omega_{i_0}|} \iint_{\Omega_{i_0}} y dx dy, \\ p^3(x, y) = x^2 - \frac{1}{|\Omega_{i_0}|} \iint_{\Omega_{i_0}} x^2 dx dy, \\ p^4(x, y) = y^2 - \frac{1}{|\Omega_{i_0}|} \iint_{\Omega_{i_0}} y^2 dx dy, \\ p^5(x, y) = xy - \frac{1}{|\Omega_{i_0}|} \iint_{\Omega_{i_0}} xy dx dy. \end{cases} \quad (21)$$

In order to obtain the high-order polynomial, the big stencil is chosen as

1. Cell average values \bar{Q} for cell 0, 1, 2, 3,
2. Cell average x gradients \bar{Q}_x for cell 1, 2, 3,
3. Cell average y gradients \bar{Q}_y for cell 1, 2, 3.

The point value of $P^2(x, y)$ at the Gaussian quadrature point (x_G, y_G) can be written as a linear combination of the cell averaged values

$$P^2(x_G, y_G) = \sum_{j=0}^3 \eta_j Q_j + \sum_{k=1}^3 \eta_l (Q_x)_k + \sum_{k=1}^3 \eta_l (Q_y)_l. \quad (22)$$

To avoid the singularity of the least square matrix, the effective technique in [17] has been adopted.

Similar with the existing WENO or HWENO reconstruction [18, 19], nine sub-stencils S_j , $j = 1, \dots, 9$ are selected from the large stencil

$$\begin{aligned} P_1^1 \text{ on } S_1 = \{i_0, i_1, i_2\}, & \quad P_2^1 \text{ on } S_2 = \{i_0, i_2, i_3\}, & \quad P_3^1 \text{ on } S_3 = \{i_0, i_1, i_3\}, \\ P_4^1 \text{ on } S_4 = \{i_0, i_1, i_{1,x}\}, & \quad P_5^1 \text{ on } S_4 = \{i_0, i_2, i_{2,x}\}, & \quad P_6^1 \text{ on } S_6 = \{i_0, i_3, i_{3,x}\}, \\ P_7^1 \text{ on } S_4 = \{i_0, i_1, i_{1,y}\}, & \quad P_8^1 \text{ on } S_4 = \{i_0, i_2, i_{2,y}\}, & \quad P_9^1 \text{ on } S_6 = \{i_0, i_3, i_{3,y}\}. \end{aligned}$$

Nine linear polynomials can be fully determined. Similarly, the point value of P_j^1 at the Gaussian quadrature point (x_G, y_G) can be written as a linear combination of the cell averaged quantities. For the linear scheme, the linear combination of P_j^1

$$R(x, y) = \sum_{j=1}^9 \gamma_j P_j^1(x, y),$$

satisfies

$$R(x_G, y_G) = P^2(x_G, y_G), \quad (23)$$

where (x_G, y_G) is the Gaussian quadrature point, and γ_j is the linear weights only depending on the local geometry of mesh. Similar with the analysis in [18], the linear system for Eq.(23) contains 10 linear equations, and generally the system is under-determined with Rank = 8. $P_j^1(x, y)$ and $P^2(x, y)$ reproduce the linear

function exactly and Eq.(23) is valid for $W(x, y) = 1$, $W(x, y) = x$, and $W(x, y) = y$ under the following identical constraint

$$\sum_{j=1}^9 \gamma_j = 1.$$

The coefficients γ_j are uniquely determined by a least square method. With the linear weights and the smooth indicator, the non-linear weights can be constructed. In order to improve the stability of the scheme, the optimization approach for the very large linear weights and the smooth indicator for the non-linear weight are used, and details can be found in [17].

Once the conservative variables at each gauss-points are constructed, a quadratic polynomial could be reconstructed using the cell average values W_0 on cell 0 and all the values of the gauss-points along the three edges of cell 0, $Q(x_{G_i}, y_{G_i}), i = 1, 2, \dots, 6$, in a least square sense. The derivatives for non-equilibrium parts could be obtained by the reconstructed quadratic polynomial. The slopes for equilibrium part are constructed by simple averages of the ones of non-equilibrium part, which seems effective in current inviscid test cases.

5 Numerical results

5.1 Numerical results of compact scheme on structured meshes

5.1.1 Accuracy tests

The advection of density perturbation is tested, and the initial condition is given as follows

$$\rho(x) = 1 + 0.2 \sin(\pi x), \quad U(x) = 1, \quad p(x) = 1, \quad x \in [0, 2].$$

The periodic boundary condition is adopted, and the analytic solution is

$$\rho(x, t) = 1 + 0.2 \sin(\pi(x - t)), \quad U(x, t) = 1, \quad p(x, t) = 1.$$

In the computation, a uniform mesh with N points is used. The time step $\Delta t = 0.2\Delta x$ is fixed. For the HWENO compact GKS, the L^1 and L^2 errors and order of accuracy at $t = 2$ are shown in Table.1. With the mesh refinement, the expected order of accuracy is obtained as well.

mesh	L^1 error	convergence order	L^2 error	convergence order
10	2.666501e-04		2.094924e-04	
20	1.082129e-05	4.6228	8.693374e-06	4.5908
40	5.530320e-07	4.2904	4.967487e-07	4.1293
80	3.251087e-08	4.0884	2.940079e-08	4.0786
160	1.971503e-09	4.0436	1.769347e-09	4.0546
320	1.210960e-10	4.0250	1.081183e-10	4.0325
640	7.497834e-12	4.0135	6.675859e-12	4.0175

Table 1: Advection of density perturbation: accuracy test for HWENO compact GKS method under smooth reconstruction.

5.1.2 One-dimensional Riemann problem

In this case, the Titarev-Toro problem is tested, in which the very high frequency wave interacts with a shock. The initial condition is given as follows

$$(\rho, U, p) = \begin{cases} (1.515695, 0.523346, 1.805), & -5 < x \leq -4.5, \\ (1 + 0.1 \sin(20\pi x), 0, 1), & -4.5 < x < 5. \end{cases}$$

The computational domain is $[-5, 5]$. The non-reflecting boundary condition is imposed on left end, and the fixed wave profile is given on the right end. Both compact GKS with HWENO and non-compact GKS with fifth-order WENO are tested for these two cases. The computed density profiles, local enlargements, and the exact solutions for the Titarev-Toro problem with 1000 mesh points at $t = 5$ are shown in Fig.1, respectively. Titarev-Toro problem is sensitive to reconstruction scheme [15]. Instead of WENO-JS used above for non-linear weights, the WENO-Z weights can keep the same order of accuracy in extreme points. Combining the HWENO-Z reconstruction with the compact GKS, the result is shown in Fig.2, which can be compared with the solution from the GRP method [11].

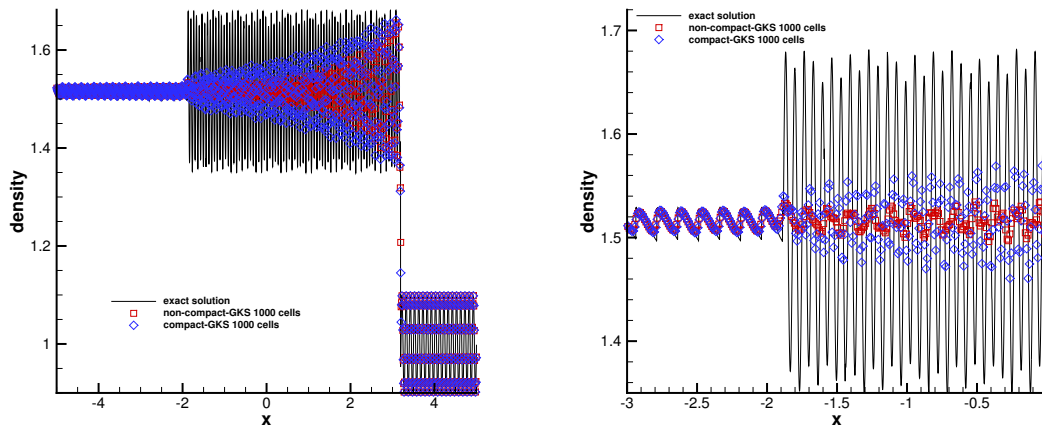


Figure 1: Titarev-Toro problem: the density distributions and local enlargement at $t = 5$ with 1000 cells.

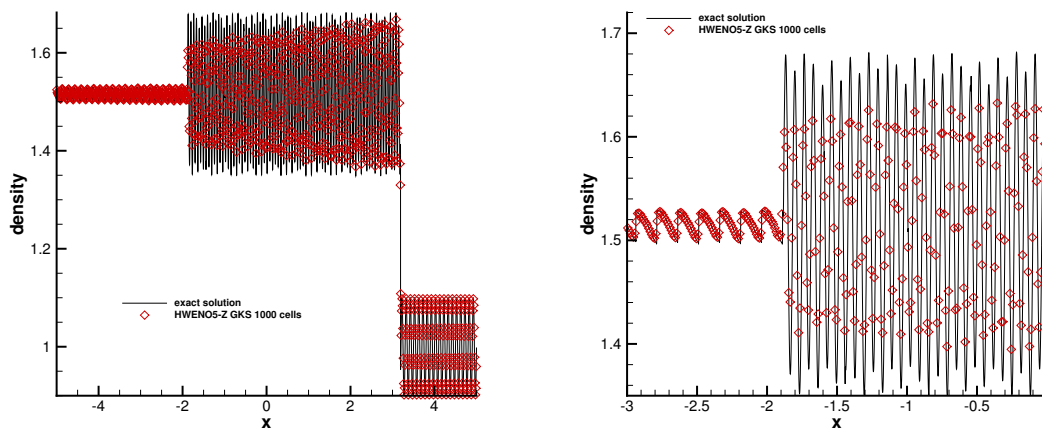


Figure 2: Titarev-Toro problem: the results by using HWENO-Z reconstruction.

5.1.3 Double Mach reflection problem

This problem was extensively studied by Woodward and Colella for the inviscid flow. The computational domain is $[0, 4] \times [0, 1]$, and a solid wall lies at the bottom of the computational domain starting from $x = 1/6$. Initially a right-moving Mach 10 shock is positioned at $(x, y) = (1/6, 0)$, and makes a 60° angle with the

x-axis. The initial pre-shock and post-shock conditions are

$$(\rho, U, V, p) = (8, 4.125\sqrt{3}, -4.125, 116.5),$$

$$(\rho, U, V, p) = (1.4, 0, 0, 1).$$

The reflecting boundary condition is used at the wall, while for the rest of bottom boundary, the exact post-shock condition is imposed. At the top boundary, the flow variables are set to follow the motion of the Mach 10 shock. The density distributions and local enlargement with 1920×480 uniform mesh points at $t = 0.2$ with HWENO reconstructions are shown in Fig.3. The robustness of the compact GKS is validated, and the flow structure around the slip line from the triple Mach point is resolved better by the compact scheme.

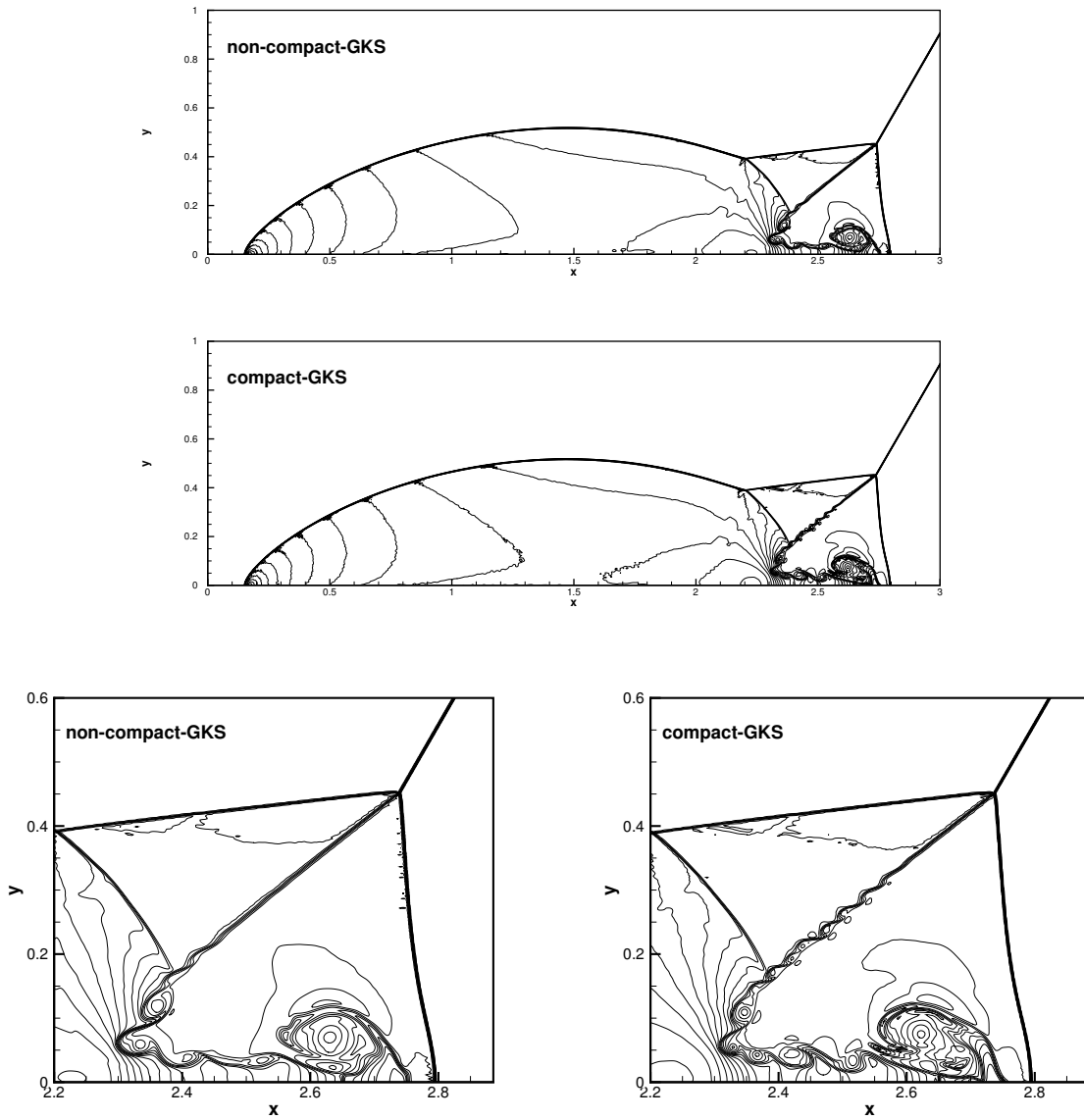


Figure 3: Double Mach reflection: local enlargement of density contours from compact and non-compact GKS with HWENO and WENO reconstructions and 1920×480 mesh points.

5.1.4 A Viscous Shock Tube

This problem was introduced to test the performances of different schemes for viscous flows [20]. In this case, an ideal gas is at rest in a two-dimensional unit box $[0, 1] \times [0, 1]$. A membrane located at $x = 0.5$ separates two different states of the gas and the dimensionless initial states are

$$(\rho, U, p) = \begin{cases} (120, 0, 120/\gamma), & 0 < x < 0.5, \\ (1.2, 0, 1.2/\gamma), & 0.5 < x < 1, \end{cases}$$

where $\gamma = 1.4$ and Prandtl number $Pr = 0.73$.

Scheme	AUSMPW+ [20]	M-AUSMPW+ [20]	WENO-GKS	HWENO-GKS
Height	0.163	0.168	0.171	0.173

Table 2: Viscous shock tube problem: comparison of the primary vortex heights among different schemes with 500×250 uniform mesh points for $Re = 200$ case.

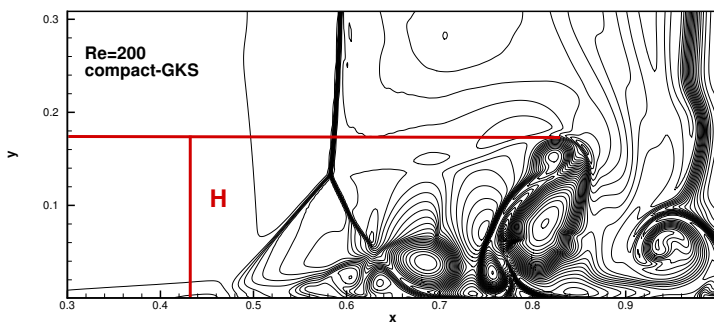


Figure 4: Viscous shock tube problem: density contours with 500×250 uniform mesh points at $t = 1$ for $Re = 200$ case.

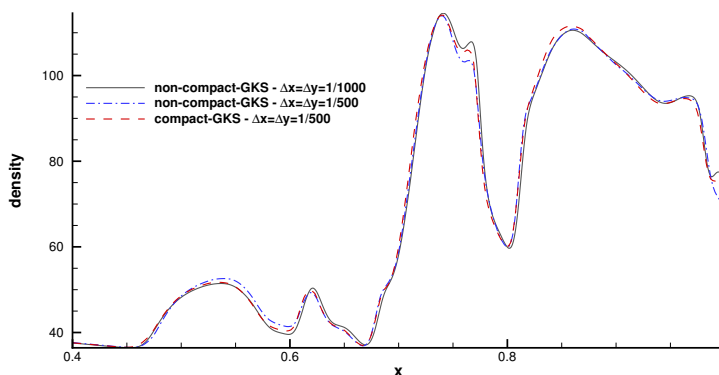


Figure 5: Viscous shock tube problem: density profiles along the lower wall at $t = 1$ for $Re = 200$ case.

The membrane is removed at time zero and wave interaction occurs. A shock wave, followed by a contact discontinuity, moves to the right with Mach number $Ma = 2.37$ and reflects at the right end wall. After the reflection, it interacts with the contact discontinuity. The contact discontinuity and shock wave interact with the horizontal wall and create a thin boundary layer during their propagation. The solution will develop complex two-dimensional shock/shear/boundary-layer interactions. This case is tested in the computational domain $[0, 1] \times [0, 0.5]$, a symmetric boundary condition is used on the top boundary $x \in [0, 1], y = 0.5$.

Non-slip boundary condition, and adiabatic condition for temperature are imposed at solid wall. Firstly, the Reynolds number $Re = 200$ case is tested. For this case with $Re = 200$, the density distributions with 500×250 uniform mesh points at $t = 1.0$ from compact GKS with HWENO reconstruction is shown in Fig.4. The density profiles along the lower wall for this case are presented in Fig.5. As a comparison, the results from WENO reconstruction with 1000×500 uniform mesh points is given as well, which agrees well with the density profiles provided by compact GKS with HWENO method and 500×250 mesh points. As shown in Table.2, the height of primary vortex predicted by the current compact scheme agrees well with the reference data [20].

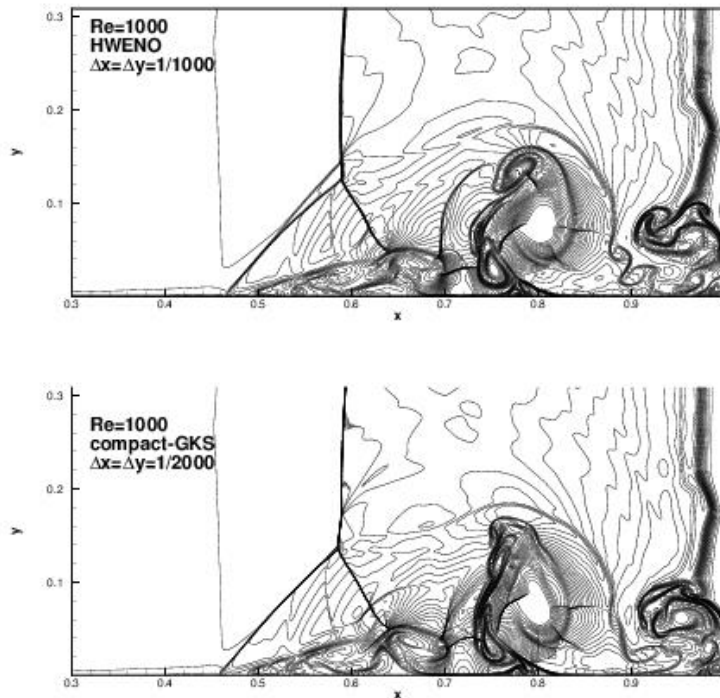


Figure 6: Viscous shock tube problem: density contours with 1000×500 and 2000×1000 uniform mesh points at $t = 1$ for $Re = 1000$.

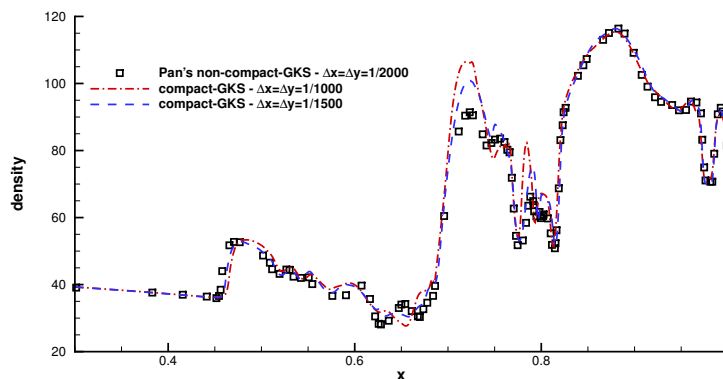


Figure 7: Viscous shock tube problem: density profiles along the lower surface at $t = 1$ for $Re = 1000$ case.

Secondly, the $Re = 1000$ case is computed with different grids. As shown in Fig.6, the vortex shedding could be observed clearly at the wedge-shaped area with 1000×500 and 2000×1000 mesh points. The

density distribution along the wall at $t = 1.0$ is plotted in Fig.7 as well. In comparison with the reference result of S2O4 GKS [1], the density distribution along the wall agree well with traditional non-compact WENO GKS.

5.2 Numerical results of compact scheme on unstructured meshes

5.2.1 Sod Problem

The standard Sod test case is used to test the mesh adaptability of the proposed scheme. The initial condition for the Sod problem is given by

$$(\rho, u, p) = \begin{cases} (1, 0, 1), & 0 < x < 0.5, \\ (0.125, 0, 0.1), & 0.5 \leq x < 1. \end{cases}$$

The computational domain is $[0, 1] \times [0, 0.5]$, and the mesh size is $h = 1/100$. Non-reflection boundary condition is adopted at the left and right boundaries of the computational domain, and periodic boundary condition is adopted at the bottom and up boundaries of the computational domain. The uniform, regular and irregular meshes are tested by the current scheme, which are given in Fig.8. The numerical results for the Sod problem at $t = 0.2$ are presented in Fig.9. Through the 3-D view of density distributions, we can see that the one-dimensional solution could be kept well by the current scheme, even when the mesh orientation is quite random.

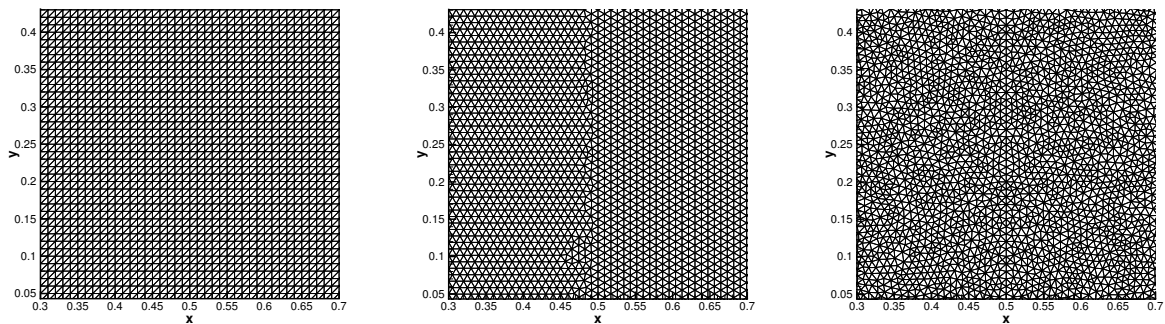


Figure 8: Sod problem: different meshes with cell size 1/100. From left to right: uniform, regular and ir-regular mesh.

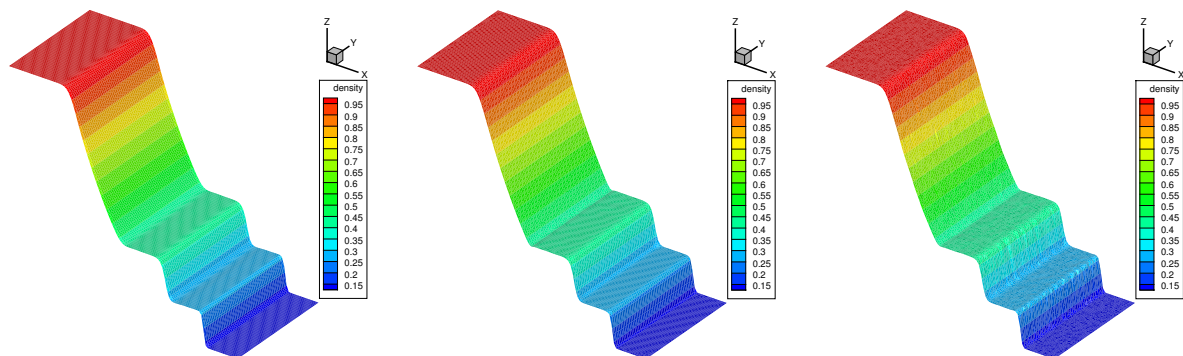


Figure 9: Sod problem: 3-D view of density distributions at $t = 0.2$ with cell size 1/100. From left to right: uniform, regular and ir-regular mesh.

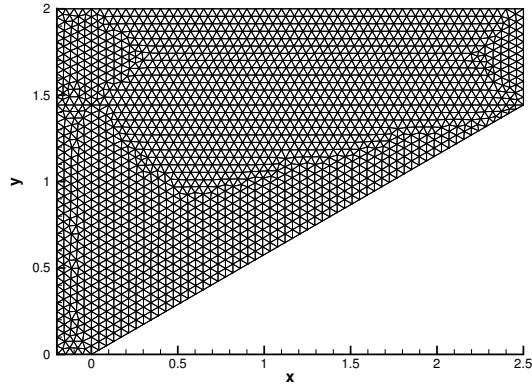


Figure 10: Double Mach reflection problem: triangular mesh sample with $h = 1/20$.

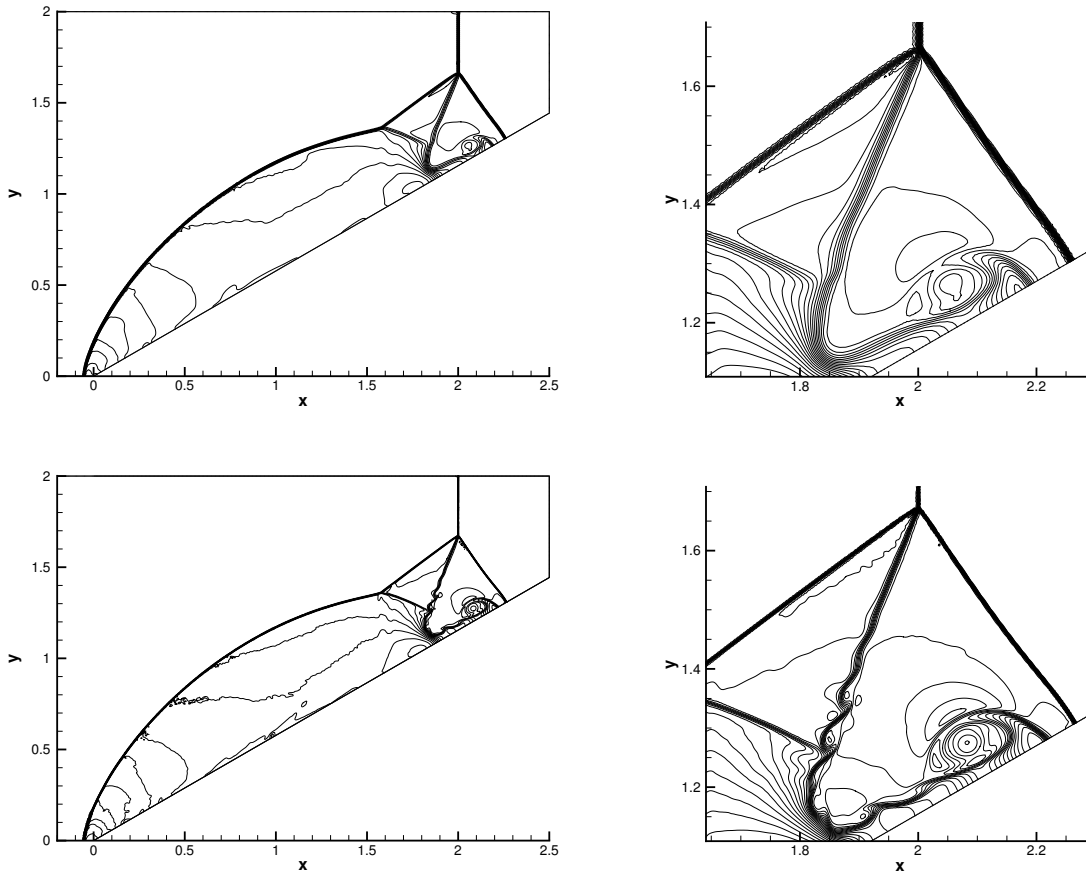


Figure 11: Double Mach reflection problem: density distributions on non-uniform meshes by compact 3rd GKS at $t = 0.2$ with $h = 1/160$, $h = 1/320$. Right: Location Enlargement.

5.2.2 Double Mach reflection problem

The double Mach reflection problem is used to test again for the performance of compact GKS on triangular mesh. A mesh sample is shown in Fig.10. The initial shock wave is imposed at $x = 0$ and parallel to y -axis with Mach number 10. The HWENO reconstruction can sustain the strong discontinues near shock

in this case. No extra low order limiter is needed. The density distributions with mesh size $h = 1/160$ and $h = 1/320$ at $t = 0.2$ are shown in Fig.11. The current scheme resolves the flow structure under the triple Mach stem nicely. The shear instabilities could be seen clearly under the fine mesh.

5.3 Numerical results for three-dimensional flows

5.3.1 Compressible homogeneous turbulence

The method is applied as a direct numerical simulations (DNS) method for the compressible decaying isotropic homogeneous turbulence. The flow is computed within a square box defined as $-\pi \leq x, y, z \leq \pi$, and the periodic boundary conditions are used in all directions for all flow variables [21]. In the computation, the domain is discretized with a uniform Cartesian mesh cells N^3 . A divergence-free random initial velocity field \mathbf{u}_0 is generated for a given spectrum with a specified root mean square u'

$$u' = \langle \frac{\mathbf{u} \cdot \mathbf{u}}{3} \rangle^{1/2},$$

where $\langle \dots \rangle$ is a volume average over the whole computational domain. The specified spectrum for velocity is given by

$$E(k) = A_0 k^4 \exp(-2k^2/k_0^2),$$

where k is the wave number, k_0 is the wave number at spectrum peaks, A is a constant chosen to get a specified initial kinetic energy. The initial volume averaged turbulent kinetic energy K_0 and the initial large-eddy-turnover time τ is given by

$$K_0 = \frac{3A_0}{64} \sqrt{2\pi} k_0^5, \quad \tau = \sqrt{\frac{32}{A_0}} (2\pi)^{1/4} k_0^{-7/2}.$$

The Taylor microscale Reynolds number Re_λ and turbulence Mach number Ma_t are given as

$$Re_\lambda = \frac{\langle \rho \rangle u' \lambda}{\langle \mu \rangle} = \frac{(2\pi)^{1/4}}{4} \frac{\rho_0}{\mu_0} \sqrt{2A_0} k_0^{3/2}, \quad Ma_t = \frac{\sqrt{3}u'}{\langle c_s \rangle} = \frac{\sqrt{3}u'}{\sqrt{\gamma T_0}},$$

where λ is Taylor microscale

$$\lambda^2 = \frac{(u')^2}{\langle (\partial_1 u_1)^2 \rangle}.$$

The dynamic viscosity is determined by

$$\mu = \mu_0 \left(\frac{T}{T_0} \right)^{0.76},$$

where μ_0 and T_0 can be determined from Re_λ and Ma_t with initialized u' and $\rho_0 = 1$. The time history of the kinetic energy, root-mean-square of density fluctuation and skewness factor for velocity slope are defined as

$$K(t) = \frac{1}{2} \langle \rho \mathbf{u} \cdot \mathbf{u} \rangle, \quad \rho_{rms}(t) = \sqrt{\langle (\rho - \bar{\rho})^2 \rangle}, \quad S_u(t) = \sum_i \frac{\langle (\partial_i u_i)^3 \rangle}{\langle (\partial_i u_i)^2 \rangle^{3/2}}.$$

In the computation, $A_0 = 1.3 \times 10^{-4}$, $k_0 = 8$, $Re_\lambda = 72$ and $Ma_t = 0.5$, and the uniform meshes with 64^3 , 96^3 and 128^3 cells are used. The iso-surfaces of Q criterion colored by velocity magnitude and the pressure distribution with $z = -\pi$ at time $t/\tau = 1$ are given in Fig.12. The time history of normalized kinetic energy $K(t)/K_0$, normalized root-mean-square of density fluctuation $\rho_{rms}(t)/Ma_t^2$ and skewness factor $S_u(t)$ with respect to t/τ are given in Fig.13. The numerical results agree well with the reference data. With fixed initial $Re_\lambda = 72$, the cases with $Ma_t = 0.2, 0.5, 0.6$ are tested, and the time histories of normalized kinetic energy $K(t)/K_0$ are given in Fig.13 as well. With the increase of Ma_t , the dynamic viscosity increases, and

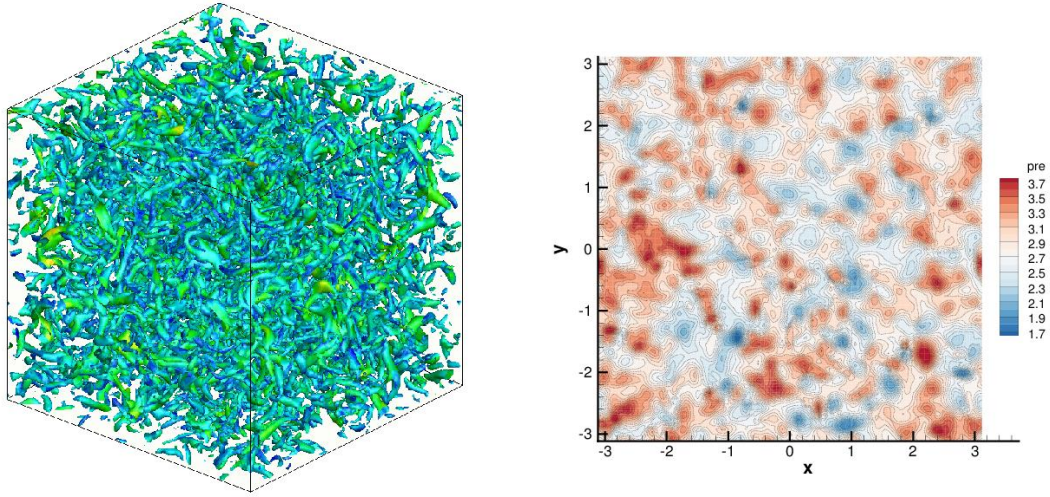


Figure 12: Compressible homogeneous turbulence. Left: iso-surfaces of Q criterion colored by velocity magnitude at time $t/\tau = 2$ with 128^3 cells; right: the pressure distribution with $z = -\pi$ at time $t/\tau = 1$.

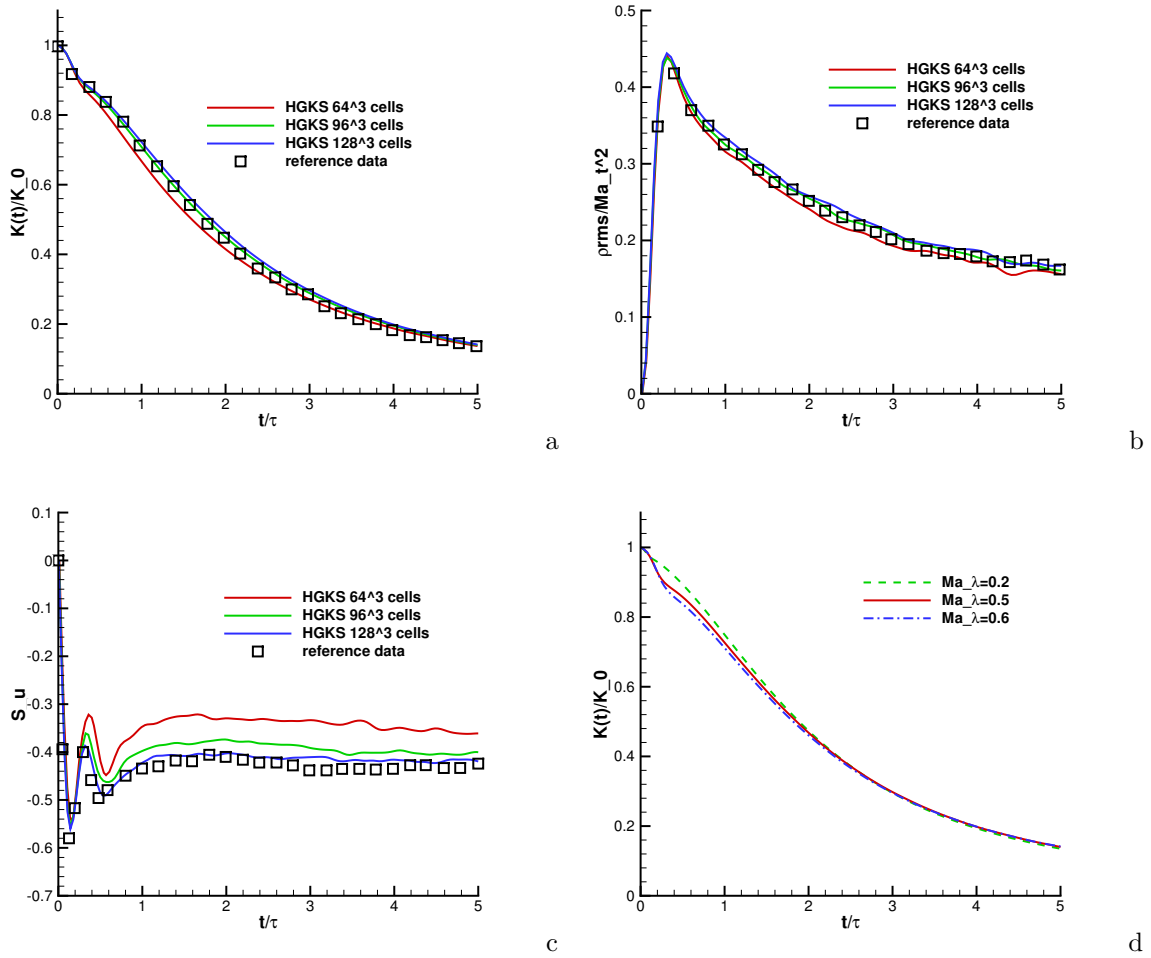


Figure 13: Compressible homogeneous turbulence: the time history of $K(t)/K_0$ (a), $\rho_{rms}(t)/Ma_t^2$ (b) and $S_u(t)$ and time history of $K(t)/K_0$ (c) with $Ma_\lambda = 0.2, 0.5$ and 0.6 with respect to t/τ (d).

the kinetic energy gets dissipated more rapidly.

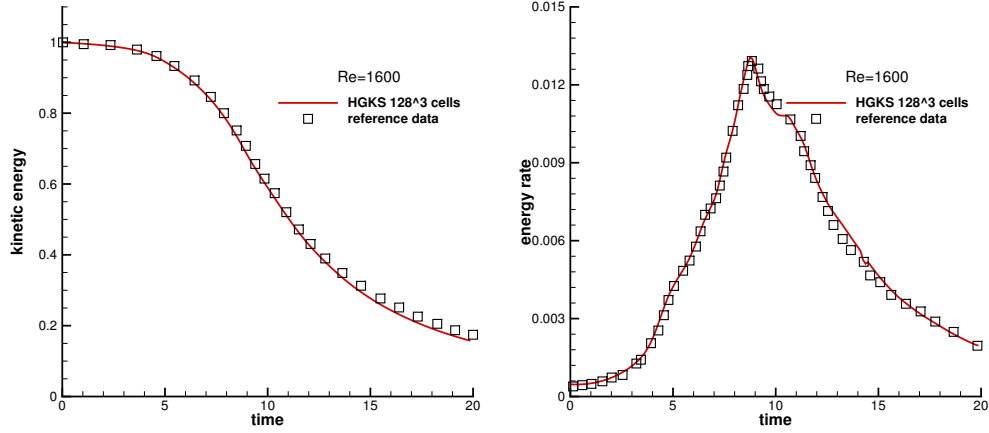


Figure 14: Taylor-Green Vortex problem: kinetic energy E_k and dissipation rate $-dk/dt$ with fourth-order scheme for $Re = 1600$.

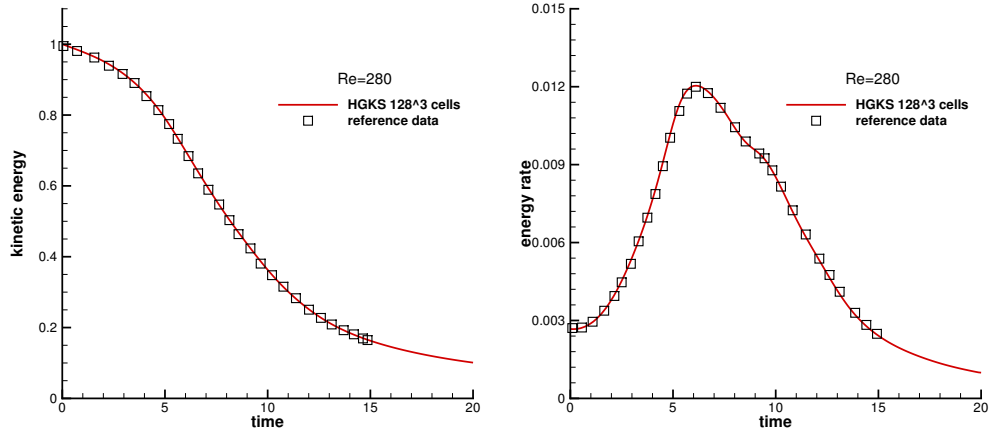


Figure 15: Taylor-Green Vortex problem: kinetic energy E_k and dissipation rate $-dk/dt$ with fourth-order scheme for $Re = 280$.

5.3.2 Taylor-Green Vortex

This problem is aimed at testing the performance of high-order methods on the direct numerical simulation of a three-dimensional periodic and transitional flow defined by a simple initial condition, i.e., the Taylor-Green vortex [22]. With a uniform temperature field, the initial flow field is given by

$$\begin{aligned}
 u &= V_0 \sin\left(\frac{x}{L}\right) \cos\left(\frac{y}{L}\right) \cos\left(\frac{z}{L}\right), \\
 v &= -V_0 \cos\left(\frac{x}{L}\right) \sin\left(\frac{y}{L}\right) \cos\left(\frac{z}{L}\right), \\
 w &= 0, \\
 p &= p_0 + \frac{\rho_0 V_0^2}{16} \left(\cos\left(\frac{2x}{L}\right) + \cos\left(\frac{2y}{L}\right) \right) \left(\cos\left(\frac{2z}{L}\right) + 2 \right).
 \end{aligned}$$

The fluid is then a perfect gas with $\gamma = 1.4$ and the Prandtl number is $Pr = 0.71$. Numerical simulations are conducted with two Reynolds numbers $Re = 1600$ and 280 . The flow is computed within a periodic square box defined as $-\pi L \leq x, y, z \leq \pi L$. The characteristic convective time $t_c = L/V_0$. In the computation, $L = 1, V_0 = 1, \rho_0 = 1$, and the Mach number takes $M_0 = V_0/c_0 = 0.1$, where c_0 is the sound speed.

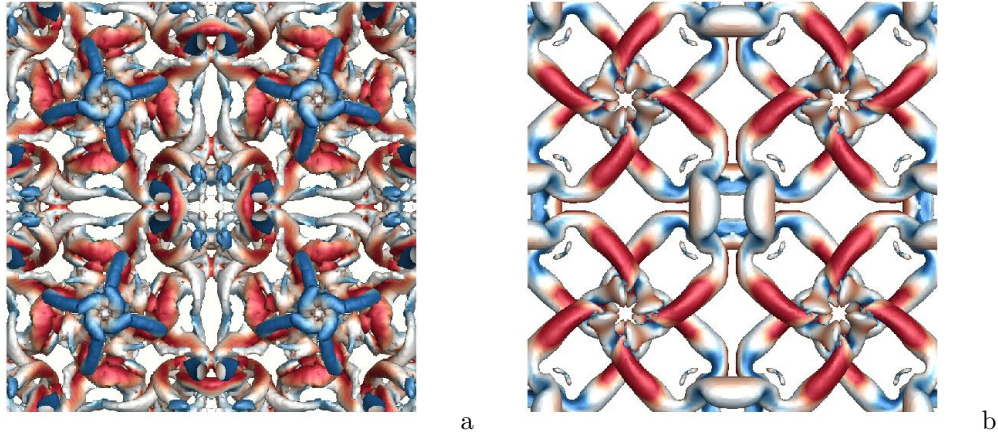


Figure 16: Taylor-Green Vortex problem: iso-surfaces of Q criterion colored by velocity magnitude at time $t = 10$ for $Re = 280$ (a) and $Re = 1600$ (b).

The volume-averaged kinetic energy can be computed from the flow as it evolves in time, which is expressed as

$$E_k = \frac{1}{\rho_0 \Omega} \int_{\Omega} \frac{1}{2} \rho \mathbf{u} \cdot \mathbf{u} d\Omega,$$

where Ω is the volume of the computational domain, and the dissipation rate of the kinetic energy is given by

$$\varepsilon_k = -\frac{dE_k}{dt}.$$

The numerical results of the current scheme with $128 \times 128 \times 128$ mesh points for the normalized volume-averaged kinetic energy and dissipation rate with Reynolds numbers $Re = 1600$ and 280 are presented in Fig.14 and Fig.15, which agree well with the data in [22]. The iso-surfaces of Q criterions colored by velocity magnitude at $t = 10$ are shown in Fig.16 for different Reynolds number. The evolution of flow structure is evident, starting from large vortices and decaying into more complex structures. Different from many other higher-order methods, the current scheme has no internal degrees of freedom to be updated within each cell.

6 Conclusion

In the paper, the two-stage fourth-order gas-kinetic scheme is extended to simulate three-dimensional flows, and a compact gas-kinetic scheme based on the HWENO reconstruction is also developed. The new advances in GKS inherit the advantages of original method, which are efficient, accurate, and robust in comparison with all currently existing higher-order schemes. The three-dimensional S2O4 GKS presents very accurate viscous flow solutions due to its multi-dimensionality in the flux evaluation at a cell interface, where the gradients in both normal and tangential directions of all flow variables participate in the gas evolution. This property is very promising for GKS to simulate complex flows, such as turbulence and acoustics with shock interactions. Accurate results are obtained as well by the current compact fourth-order GKS with high efficiency. Only 2-stages are used for the fourth-order accuracy in time due to the use of both flux and its time derivative, and the time step used here in almost all calculations are on the order of CFL number 0.5. On the contrary, the popular compact 4th-order DG method with the same HWENO limiter [23] needs four stages within each time step to get a 4th-order temporal accuracy, and the time step for the DG method is on the order of CFL number 0.11 from the stability consideration. This distinguishable feature is solely from the updated slopes in GKS through the explicit time evolution solution of flow variables at the cell interfaces, and the updated slope is based on the evolution solution at the cell interface, instead of updating the slopes (weak solution) directly inside each cell in the HWENO DG method. Here, the slope in GKS

is obtained through the Gauss's theorem at the beginning of the new time step. The HWENO is fully implemented without using any additional trouble cell detection and limiting technique. As a result, the 4th-order compact GKS has the same robustness as the 2nd-order shock capturing scheme. On unstructured mesh, combining two-stage time stepping method and HWENO reconstruction, a third-order spatial and temporal accurate compact GKS can be constructed. The proposed scheme shows good mesh adaptivity even for a highly irregular mesh through a carefully designed optimized linear weights.

Acknowledgement

The current research was supported by Hong Kong research grant council (16206617,16207715) and NSFC (Grant Nos. 11772281,91530319).

References

- [1] Liang Pan, Kun Xu, Qibing Li, and Jiequan Li. An efficient and accurate two-stage fourth-order gas-kinetic scheme for the Euler and Navier–Stokes equations. *Journal of Computational Physics*, 326:197–221, 2016.
- [2] Jun Luo and Kun Xu. A high-order multidimensional gas-kinetic scheme for hydrodynamic equations. *Sci. China, Technol. Sci*, 56(10):2370–2384, 2013.
- [3] Kun Xu. A gas-kinetic BGK scheme for the Navier–Stokes equations and its connection with artificial dissipation and Godunov method. *Journal of Computational Physics*, 171(1):289–335, 2001.
- [4] Prabhu Lal Bhatnagar, Eugene P Gross, and Max Krook. A model for collision processes in gases. i. Small amplitude processes in charged and neutral one-component systems. *Physical review*, 94(3):511, 1954.
- [5] Qibing Li, Kun Xu, and Song Fu. A high-order gas-kinetic Navier–Stokes flow solver. *Journal of Computational Physics*, 229(19):6715–6731, 2010.
- [6] Kun Xu, Meiliang Mao, and Lei Tang. A multidimensional gas-kinetic BGK scheme for hypersonic viscous flow. *Journal of Computational Physics*, 203(2):405–421, 2005.
- [7] Xing Ji, Fengxiang Zhao, Wei Shyy, and Kun Xu. A family of high-order gas-kinetic schemes and its comparison with riemann solver based high-order methods. *Journal of Computational Physics*, 356:150–173, 2018.
- [8] Liang Pan and Kun Xu. A third-order gas-kinetic scheme for three-dimensional inviscid and viscous flow computations. *Computers & Fluids*, 119:250–260, 2015.
- [9] Liang Pan and Kun Xu. A third-order compact gas-kinetic scheme on unstructured meshes for compressible Navier–Stokes solutions. *Journal of Computational Physics*, 318:327–348, 2016.
- [10] Jianxian Qiu and Chi-Wang Shu. Hermite WENO schemes and their application as limiters for Runge–Kutta discontinuous Galerkin method: one-dimensional case. *Journal of Computational Physics*, 193(1):115–135, 2004.
- [11] Zhifang Du and Jiequan Li. A hermite weno reconstruction for fourth order temporal accurate schemes based on the grp solver for hyperbolic conservation laws. *Journal of Computational Physics*, 355:385–396, 2018.
- [12] Kun Xu. *Direct modeling for computational fluid dynamics: construction and application of unified gas-kinetic schemes*. World Scientific, 2014.
- [13] Jiequan Li and Zhifang Du. A two-stage fourth order time-accurate discretization for Lax–Wendroff type flow solvers I. hyperbolic conservation laws. *SIAM Journal on Scientific Computing*, 38(5):A3046–A3069, 2016.
- [14] Guang-Shan Jiang and Chi-Wang Shu. Efficient implementation of weighted ENO schemes. *Journal of computational physics*, 126(1):202–228, 1996.
- [15] Rafael Borges, Monique Carmona, Bruno Costa, and Wai Sun Don. An improved weighted essentially non-oscillatory scheme for hyperbolic conservation laws. *Journal of Computational Physics*, 227(6):3191–3211, 2008.
- [16] Guangzhao Zhou, Kun Xu, and Feng Liu. Simplification of the flux function for a high-order gas-kinetic evolution model. *Journal of Computational Physics*, 339:146–162, 2017.

- [17] Fengxiang Zhao, Liang Pan, and Shuanghu Wang. Weighted essentially non-oscillatory scheme on unstructured quadrilateral and triangular meshes for hyperbolic conservation laws. *arXiv preprint arXiv:1712.08317*, 2017.
- [18] Changqing Hu and Chi-Wang Shu. Weighted essentially non-oscillatory schemes on triangular meshes. *Journal of Computational Physics*, 150(1):97–127, 1999.
- [19] Jun Zhu and Jianxian Qiu. Hermite weno schemes and their application as limiters for runge-kutta discontinuous galerkin method, iii: unstructured meshes. *Journal of Scientific Computing*, 39(2):293–321, 2009.
- [20] Kyu Hong Kim and Chongam Kim. Accurate, efficient and monotonic numerical methods for multi-dimensional compressible flows: Part II: Multi-dimensional limiting process. *Journal of computational physics*, 208(2):570–615, 2005.
- [21] Wei Liao, Yan Peng, and Li-Shi Luo. Gas-kinetic schemes for direct numerical simulations of compressible homogeneous turbulence. *Physical Review E*, 80(4):046702, 2009.
- [22] James DeBonis. Solutions of the taylor-green vortex problem using high-resolution explicit finite difference methods. In *51st AIAA Aerospace Sciences Meeting including the New Horizons Forum and Aerospace Exposition*, page 382, 2013.
- [23] Jianxian Qiu and Chi-Wang Shu. Hermite weno schemes and their application as limiters for runge-kutta discontinuous galerkin method ii: Two dimensional case. *Computers & Fluids*, 34(6):642–663, 2005.